Acta Pharmaceutica Sinica B 2026;16(1):522−538

Chinese Pharmaceutical Association
Institute of Materia Medica, Chinese Academy of Medical Sciences

Acta Pharmaceutica Sinica B

www.elsevier.com/locate/apsb
www.sciencedirect.com

ORIGINAL ARTICLE

Engineered bacterial extracellular vesicles mediate pyroptosis to counteract m^{6}A methylation-based immunosuppression after insufficient radiofrequency ablation of hepatocellular carcinoma

Zeyu Xiao[a,†,*], Jiaxin Yuan[a,†], Qing Wu[e,†], Juan Qin[c], Yiming Liu[c], Siqi Zhang[d], Bo Sun[a], Ruoxue Dai[a], Pingping Zhang[a], Ni Shao[a], Shuang Che[a], Yin He[a], Jifeng Chen[a], Shunqian Wen[e], Kuan Hu[d,*], Duo Wang[c,*], Liangping Luo[b,*]

[a]*The Guangzhou Key Laboratory of Molecular and Functional Imaging for Clinical Translation, Department of Radiology and Nuclear Medicine, The First Affiliated Hospital of Jinan University, Guangzhou 510630, China*
[b]*Department of Radiology and Nuclear Medicine, The Fifth Affiliated Hospital of Jinan University (Shenhe People's Hospital), Heyuan 517000, China*
[c]*Center of Interventional Radiology & Vascular Surgery, Department of Radiology, Zhongda Hospital, Medical School, Southeast University, Nanjing 210009, China*
[d]*State Key Laboratory of Bioactive Substance and Function of Natural Medicines, Institute of Materia Medica, Chinese Academy of Medical Sciences & Peking Union Medical College, Beijing 100050, China*
[e]*Department of Hepatic-Biliary-Pancreatic Surgery, The Second People's Hospital of Foshan, Foshan 528000, China*

Received 14 February 2025; received in revised form 16 July 2025; accepted 7 August 2025

KEY WORDS

Hepatocellular carcinoma;
Insufficient

Abstract Insufficient radiofrequency ablation (IRFA) of hepatocellular carcinoma (HCC) leads to alterations in epigenetic properties such as N^6-methyladenosine (m^{6}A) RNA methylation in tumor cells, which creates an immune-suppressive tumor microenvironment capable of promoting residual tumor

*Corresponding authors.
E-mail addresses: zeyuxiao@jnu.edu.cn (Zeyu Xiao), hukuan@imm.ac.cn (Kuan Hu), wangduo2022@126.com (Duo Wang), tluolp@jnu.edu.cn (Liangping Luo).
†These authors made equal contributions to this work.
Peer review under the responsibility of Chinese Pharmaceutical Association and Institute of Materia Medica, Chinese Academy of Medical Sciences.

https://doi.org/10.1016/j.apsb.2025.11.005

radiofrequency ablation;
Tumor immune microenvironment;
N^6-methyladenosine RNA methylation;
Pyroptosis;
Outer membrane vesicles;
STING;
YTHDF1

growth and recurrence and affecting the efficacy of RFA. In this study, the constructed STM-Mn@OMVs, which were produced through the rational functionalisation of bacterial-derived OMVs with Mn^{2+} ions and the methylation inhibitor STM2457, were found to effectively activate antitumor immunity. Our study shows that STM-Mn@OMVs can effectively promote dendritic cells (DCs) maturation, T cell activation, and STING pathway activation after endocytosis by cells, thus promoting immune cell infiltration. The STM-Mn@OMVs were able to promote cellular pyroptosis and synergistically activate the STING pathway. Furthermore, STM-Mn@OMVs promoted the increase of M1 macrophage phenotype in tumor-associated macrophages (TAMs) by reducing the infiltration of immunosuppressive cell populations such as regulatory T cells (Tregs) and myeloid-derived suppressor cells (MDSCs), thus reversing the suppressive immune microenvironment after IRFA to some extent. Ultimately, the growth of residual tumors was inhibited. In addition, the biosafety of STM-Mn@OMVs was demonstrated in this study. Therefore, the STM-Mn@OMVs constructed in this study have great potential for application in the field of RFA and immunotherapy for HCC.

1. Introduction

Radiofrequency ablation (RFA) represents a significant advancement in the treatment of HCC and is currently recommended by the American Association for the Study of Liver Diseases as a treatment for early-stage HCC[1,2]. However, insufficient RFA (IRFA) elevates the probability of tumor recurrence[3]. During the RFA procedure, the central zone is defined as the temperature exceeding 50 °C, which is capable of inducing coagulation denaturation or necrosis to kill tumor cells[4]. While cells in non-lethal temperatures of the transition zone exposed to sub-lethal heat stress at temperatures ranging between 41 and 50 °C are capable of inducing dynamic epigenetic changes in tumor cells, leading to the expression of stress-responsive genes, which maintain cellular homeostasis and survival[4-6].

Research indicates that the N^6-methyladenosine (m^{6}A) mRNA-YTH m^{6}A RNA-binding protein 1 (YTHDF1)-epidermal growth factor receptor (EGFR) axis plays a promoting role in the recurrence and progression of HCC after IRFA[7]. After IRFA treatment, the m^{6}A methylation modification level in HCC tumor cells significantly increased, which in turn led to the upregulation of YTHDF1 expression, thereby promoting the recurrence and progression of HCC by upregulating EGFR expression. Meanwhile, the METTL3 in the cytoplasm of HCC cells translocated to the nucleus in large quantities, enabling it to bind to more mRNAs and exert a stronger m^{6}A catalytic activity. m^{6}A RNA methylation has been demonstrated to be a pivotal factor in the development and progression of numerous tumors, including HCC[8,9]. In addition, residual tumor cells after IRFA are able to induce infiltration of myeloid-derived suppressor cells (MDSCs) and tumor-associated macrophages (TAMs), leading to persistent local inflammation[10]. The upregulation of MDSCs is able to inhibit T-cell function in the tumor, thereby suppressing the anti-inflammatory effects of the tumor immune microenvironment (TIME) and accelerating the progression of the residual tumor[11,12]. Therefore, in response to the clinical need to reduce tumor recurrence after IRFA, there is an urgent need to develop a combined immunotherapy strategy that is easy to implement in clinical practice, has significant efficacy, and has few side effects. This strategy can effectively curb the local chronic inflammation caused by sublethal thermal stress in the transition zone by inhibiting m^{6}A methylation and actively regulating the tumor immune microenvironment (TIME), thereby further enhancing the clinical efficacy of RFA.

Nanomaterials offer significant advantages in immunotherapy due to their precise delivery capabilities, multifunctionality, and potential to synergistically activate the immune system[13-16]. While biological nanoparticles of natural origin have important applications in tumor therapy, they also contribute to the excellent biocompatibility and functionality. Among these, outer membrane vesicles (OMVs) of Gram-negative bacterial origin, as an emerging biocarrier, show potential in drug delivery, tumor targeting, and immunomodulation[17]. The presence of multiple pathogen-associated molecular patterns (PAMPs), such as peptidoglycans, lipopolysaccharides (LPSs), and flagellin, in OMVs possesses the potent ability to activate innate immune signalling pathways[18]. They are capable of activating intracellular signalling through ligand−receptor interactions and/or being internalised by target cells through endocytosis, phagocytosis, micropinocytosis, or membrane fusion[19]. It has been demonstrated that OMVs can activate the NLRP3 inflammatory vesicle signalling pathway *via* Caspase-11, upregulate IL-1β secretion[20], and promote T cell maturation and its mediated adaptive immune response[21,22]. And the activation of NLRP3 inflammatory vesicle can lead to the cleavage and activation of pro-Caspase-1[23], while the activated Caspase-1 is a key enzyme in the process of cellular pyroptosis[24]. Furthermore, the LPS of OMVs can induce the onset of cellular pyroptosis through a non-classical pathway, resulting in the release of antigens and inflammatory factors (including IL-1β) in tumor cells[25]. At the same time, proinflammatory cytokines are beneficial in reversing the immune-suppressive tumor microenvironment and enhancing antitumor immunity[26,27]. Despite the considerable efforts of numerous researchers to investigate the potential of OMVs in tumor immunotherapy, research into HCC remains underexplored.

In view of the aforementioned background, the aim of our study was to design and develop a radiofrequency sensitising adjuvant based on OMVs that would be beneficial in enhancing the immune response and reducing tumor recurrence following IRFA. In previous studies, we have demonstrated that Mn^{2+} ions activate the cGAS/STING pathway, which significantly enhances antitumor immunity[28]. A series of related studies have been conducted on the STING pathway[29]. Moreover, evidence suggests that the STING pathway has the capacity to reverse the immune-suppressive

tumor microenvironment in HCC, enhance the effect of immune checkpoint inhibitors, and reduce tumor recurrence[30]. Given the role of Mn^{2+} in activating the STING pathway and enhancing MRI T1-weighted imaging signals, and considering the key regulatory role of m^6A RNA methylation in tumor recurrence after IRFA, we developed a strategy to co-load Mn^{2+} ions and an m^6A methylation inhibitor (STM2457) mainly targeting METTL3 methyltransferase onto OMVs. This approach aims to enhance antitumor immunity while attenuating the sub-lethal heat stress effect after IRFA. The results demonstrate that following systemic injection, the prepared STM-Mn@OMVs were capable of markedly enhancing the immune response following IRFA in the mouse HCC model. This resulted in a robust antitumor response without evident side effects. By regulating m^6A RNA methylation, activating the STING pathway, inducing pyroptosis, and reversing the immune-suppressive tumor microenvironment, this novel adjuvant provides new ideas and strategies for the treatment of HCC with tremendous potential for clinical application.

2. Materials and methods

Detailed descriptions of the material synthesis, animal models employed, and experimental methodologies utilized in this study are provided in the Supporting Information

2.1. Study design

The primary objective of this study was to test the hypothesis that OMVs carrying Mn^{2+} ions and STM2457 (STM-Mn@OMVs), administered intravenously, could enhance the immune response of HCC following IRFA and inhibit the growth of residual tumors. In this study, we used the Hepa1-6 mouse model of HCC to assess the therapeutic effect of STM-Mn@OMVs by comparing tumor size, survival, and changes in the TIME in different groups. We quantified and immunophenotyped endogenous and peripherally transfected tumor-infiltrating T-cell populations to assess the reversal of immunosuppression. Immunofluorescence and Western blotting were used to analyse cGAS/STING pathway activation as well as cellular pyroptosis in the tumor microenvironment. Before starting treatment, all mice were randomly assigned to different groups. The study ended when mice showed signs of serious health problems or when the tumor size was equal to or greater than 1000 mm^3. Tumor size assessment was performed anonymously where feasible. Each experiment was conducted a minimum of three times (Scheme 1).

2.2. Cell lines and animals

The cells employed in this study were Hepa1-6, obtained from ATCC and cultivated in the recommended medium and conditions, in strict adherence to the prescribed procedure. The animal experiments were conducted using 6- to 8-week-old C57BL/6 mice sourced from SPF Biotech (Beijing, China). All experimental procedures were performed in strict accordance with the established guidelines and were approved by the Animal Ethics Committee of Jinan University (IACUC-20240104-06).

2.3. Animal models and treatments

In this study, an *in vivo* model of the antitumor effect of STM@OMVs was established through the subcutaneous inoculation of 1×10^6 Hepa1-6 cells into C57BL/6 mice. An orthotopic liver tumor model was also established to evaluate the antitumor efficacy of STM@OMVs by inoculating 1×10^6 Hepa1-6 cells into the liver parenchyma at a depth of approximately 3 mm using a syringe, followed by slow and controlled injection to ensure localized cell deposition.

IRFA treatment of the Hepa1-6 tumor mice (subcutaneous inoculation): after 7 days of culture of the tumor mice, the tumors grew to approximately 150 mm^3. The mice were randomly divided into different groups. The group without IRFA is the control group, while the experimental group needs to be treated with IRFA. RFA was performed using a 17-gauge single ablation electrode (RITA Medical Systems Inc., Mountain View, CA, USA) inserted percutaneously into a 1 cm active tip. The power was set at 7 W, and the electrode tip was positioned at the midpoint of the tumor's long axis. The treatment time was 1.5 to 2.0 min, with the target temperature set at 70 °C. The objective was to induce partial necrosis of the tumor in order to achieve IRFA[10]. The specific subgroups of the IRFA group and the corresponding modes of administration are described in detail below.

The Hepa1-6 tumor-bearing mice (hepatic in orthotopic model) were cultured for a period of seven days, during which time the tumors exhibited growth to an approximate volume of 150 mm^3. The mice were randomly divided into two groups ($n = 5$), and both groups were pre-treated with IRFA according to the aforementioned procedure. On the first day after IRFA, the IRFA group was injected with PBS, while the STM@OMVs group was injected with STM@OMVs.

During the assessment period following administration of the Hepa1-6 tumor-bearing mice model, the tumor volume, body weight, and survival rate of the mice were monitored and recorded at 2-day intervals. The IVIS Lumina imaging system (Caliper Life Science, MA, USA) was used to track tumor growth using bioluminescent signals emitted by tumor cells. The study ended when mice showed signs of serious health problems or when the tumor size was equal to or greater than 1000 mm^3. Blood samples, tumor tissues, major organs, and draining lymph nodes of mice were collected for further study.

2.4. Immunoactivation analysis of the components of the material

In order to clarify and validate the effect of each component of our prepared materials on immune activation, we first validated the role of each component of the materials in promoting DCs maturation and STING pathway activation. The Hepa1-6 subcutaneous tumor-bearing mice were cultured for a period of seven days and then randomly divided into seven groups, of which six groups were pre-treated with IRFA, and the group without IRFA was designated as the control group. The IRFA pre-treated group was injected intravenously with PBS, OMVs, Mn^{2+}, STM2457, a mixture (simply mixing STM2457, OMVs, and Mn^{2+}), and STM-Mn@OMVs, respectively, on Day 1 after IRFA. At the same time, the control group was injected with PBS. DC cell maturation in tumor-draining lymph nodes was analyzed by flow cytometry after 3 days of treatment. Western blot analysis was also conducted to assess the activation of the STING pathway in tumor cells, with the expression of STING, p-STING, IRF3, p-IRF3, TBK1, and p-TBK1. After 3 days of treatment, the concentrations of IL-1β, IL-6, TNF-α, and IL-12p70 in serum were quantified by ELISA in blood samples obtained from mice. Then, the mice were

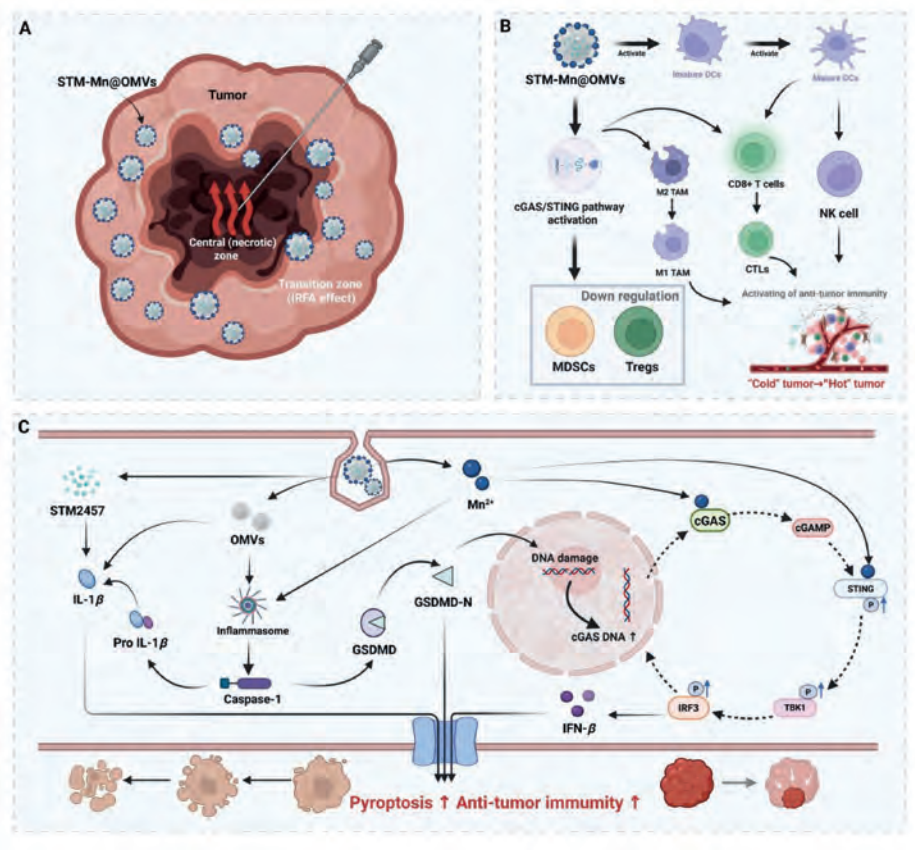

Scheme 1 Schematic diagram representation of residual hepatocellular carcinoma anti-tumor immunity after enhancement of IRFA by STM-Mn@OMVs. (A) Aggregation of STM@OMVs to residual tumor sites after IRFA in hepatocellular carcinoma. (B) Anti-tumor immunity is activated after treatment with STM-Mn@OMVs, which convert "Cold" tumors into "Hot" tumors. (C) STM-Mn@OMVs induces tumor cellular pyroptosis, synergistically activating the cGAS−STING pathway. This figure was created in BioRender. Jiaxin, Y. (2025) https://BioRender.com/p59y584.

euthanised, and the tumor tissues were collected and filtered through a 40 μm nylon mesh to create a single-cell suspension, and the infiltration of $CD3^+CD8^+$ lymphocytes was analyzed by flow cytometry.

2.5. *Therapeutic efficacy and immune response analysis*

Assessment of treatment efficacy: the Hepa1-6 subcutaneous tumor-bearing mice were cultured for a period of seven days and then randomly divided into six groups, of which five groups were pre-treated with IRFA, and the group without IRFA was designated as the control group. The IRFA pre-treated group was injected intravenously with PBS, OMVs, Mn@OMVs, STM@OMVs, and STM-Mn@OMVs. At the same time, the control group was injected with PBS. The tumor volume, body weight, and survival rate of the mice were monitored and recorded at 2-day intervals. Tumor tissues were collected after 14 days of treatment for H&E, Ki-67, TUNEL staining, and Western blot analysis.

Immune cell infiltration and pyroptosis analysis: in the Hepa1-6 tumor-bearing mice (subcutaneous inoculation) model, after 7 days of treatment, the tumor tissues were collected. Expression of IL-1β, Gasdermin D (GSDMD), cleaved GSDMD-N, pro-Caspase-1, and cleaved-Caspase-1 in tumor cells was analysed by Western blot for clear activation of pyroptosis. Immune activation after treatment was assessed by flow cytometry analysis of the infiltration of different types of immune cells into the tumor tissue and ELISA analysis of the production of corresponding cytokines such as Interferon-gamma (IFN-γ), Granzyme B (GZMB), tumor Necrosis Factor-alpha (TNF-α), Forkhead box P3 (Foxp3), Transforming Growth Factor-beta (TGF-β), and so on.

Immune activation in orthotopic model: We further verified the immune activation and efficacy of the drug in the Hepa1-6 tumor-bearing mice (orthotopic HCC model). The mice were euthanized, and the tumor tissues were collected for sectioning and staining after the corresponding treatment period. After 7 days of treatment, blood samples were collected to quantify serum levels of TNF-α and IFN-γ. In addition, the tumor tissues were also obtained for flow cytometry analysis of tumor cells and staining by Western blotting. We also detected tumor cell proliferation (Ki-67) and apoptosis (TUNEL method[31]).

2.6. *Biosafety*

The biosafety assessment is divided into blood biochemistry (liver and kidney function) and post-treatment organ examination.

Post-treatment organ examination: Hepa1-6 tumor-bearing mice were divided into six groups ($n = 5$) with the following treatment protocols. (1) control group, tail vein injection of PBS buffer. (2)−(5) groups were all treated with IRFA, where (2) was

injected with PBS buffer; (3) was injected with OMVs; (4) was injected with Mn@OMVs; (5) was injected with STM@OMVs; and (6) was injected with STM-Mn@OMVs. The deposition of Mn^{2+} in various organs and tumor tissues was quantitatively assessed by ICP-OES 14 days after treatment in the STM-Mn@OMVs group. Following the above experimental protocols, organs (heart, lung, liver, spleen, and kidney) from each group were collected 14 days post-treatment, fixed in 4% paraformaldehyde, and embedded in paraffin to prepare four μm-thick tissue sections. The sections were deparaffinised, hydrated, and stained with haematoxylin and eosin for 2−5 min. After staining, the sections were rinsed with water and embedded in resin for rehydration. PerkinElmer evaluated pathological changes using the automated quantitative pathology imaging system.

Blood biochemistry analysis (liver and kidney function): to evaluate the drug safety of STM-Mn@OMVs, the healthy mice were randomly divided into two groups ($n = 3$). (1) a control group treated with PBS *via* the tail vein and (2) an STM-Mn@OMVs group treated with STM-Mn@OMVs *via* the tail vein. Blood samples were taken 30 days after drug administration, and serum was extracted and centrifuged at 860 rpm (Dynamica Velocity 14R PRO). In addition, organs (heart, lung, liver, spleen, and kidney) were collected and pathological changes were assessed as described above. A number of biochemical parameters, including alanine aminotransferase (ALT), aspartate aminotransferase (AST), albumin (ALB), creatinine (CREA), urea, γ-glutamyltransferase (γ-GT), creatine kinase (CK), and lactate dehydrogenase (LDH), were measured using a fully automated biochemical analyser.

2.7. Statistical analysis

The results are compared using unpaired Student's t-tests and expressed as mean ± standard deviation (SD), as indicated. The log-rank (Mantel-Cox) test was employed to analyze statistical differences in survival rates. Statistical analysis was performed using MedCalc software (MedCalc Software Ltd., Ostend, Belgium) and GraphPad Prism 9.0 Software for Windows (GraphPad Software, San Diego, CA, USA). (ns, not significant, $*P < 0.05$, $**P < 0.01$, $***P < 0.001$).

3. Results

3.1. Characterization of STM-Mn@OMVs

STM-Mn@OMVs characteristics: the schematic of the synthesis of STM-Mn@OMVs is shown in Fig. 1A. The morphology of OMVs, STM@OMVs, Mn@OMVs, and STM-Mn@OMVs was observed to be spherical by TEM (Fig. 1B). In addition, the mean diameter of each material synthesised approximates that of the OMVs, which are approximately 100 nm (Fig. 1C). This finding indicates that the loading of the drug does not result in a substantial alteration in the size of the OMVs. Elemental mapping analysis of STM-Mn@OMVs confirms the presence of C, N, O, P, and Mn elements (Supporting Information Fig. S1). The drug encapsulation efficiency of Mn^{2+} was quantified using inductively coupled plasma optical emission spectrometry (ICP-OES), yielding a value of 56.8%. Concurrently, the encapsulation efficiency of STM2457 was analyzed *via* high-performance liquid chromatography (HPLC), resulting in a value of 62.4%. In this study, we employed MRI to monitor the alterations in the T1-weighted signal of STM-Mn@OMVs following 24 h of intratumor (i.t.) administration. The T1-weighted images (Fig. 1D) demonstrated that the T1-weighted signals in the STM-Mn@OMVs group underwent gradual enhancement at 6, 12, and 24 h following drug administration, thereby indicating that the drug was capable of significant enrichment within the tumor. Furthermore, the treatment of STM-Mn@OMVs demonstrated a reduction in T1 relaxation time and an enhancement in T1-weighted signals in comparison to free Mn^{2+} (Fig. 1E), thereby further substantiating the hypothesis that STM-Mn@OMVs exhibited a greater retention of free Mn^{2+} within the tumor region. Subsequently, we investigated the pH-responsive drug release behaviors of STM-Mn@OMVs. The pH values were set to 7.4 and 6.5 to simulate drug release under normal physiological conditions and in the acidic microenvironment of tumors, respectively. The results demonstrate that Mn^{2+} and STM2457 of STM-Mn@OMVs exhibited rapid release at a pH of 6.5, with a significantly higher percentage of release compared to pH 7.4 (Fig. 1F and G). This phenomenon may be attributed to the decreased membrane stability of OMVs under acidic conditions[32], as well as the change in permeability due to alterations in protein conformation[33]. To further evaluate the membrane stability of OMVs under varying pH conditions, we monitored the temporal changes in OMV size across different pH levels (Supporting Information Fig. S2). The results reveal that at pH 6.5, OMVs exhibited a gradual increase in size over time, indicating potential vesicle swelling, aggregation, and fusion. In contrast, at pH 7.4, the vesicle size remained largely unchanged. These observations demonstrate that OMVs maintain favorable membrane stability under the normal physiological pH of the human body (7.4), whereas their structural integrity is compromised in the acidic tumor microenvironment, which may promote enhanced drug release. The *in vitro* optimal dose gradient experiment demonstrated that STM-Mn@OMVs induced a dose-dependent decrease in cell viability in Hepa1-6 cells (Supporting Information Fig. S3). Consequently, the present study demonstrates that the prepared STM-Mn@OMVs not only exhibit significant tumor enrichment and enhance the T1-weighted MRI signals, but also possess pH-responsive therapeutic release properties and exert *in vitro* therapeutic effects. These findings provide strong evidence for the therapeutic potential of STM-Mn@OMVs in tumor-specific therapy.

Immune activation of the components of STM-Mn@OMVs: OMVs have been shown to have a strong ability to be activators of innate immune pathways[18], while Mn^{2+} has also been shown to activate the cGAS−STING pathway[34]. In order to investigate the effect of the different components of our designed material on the immune activation aspect, we collected tumor-draining lymph nodes and tumor tissue three days after drug administration in the mouse model and analyzed them separately.

We analysed dendritic cells (DCs) maturation in the mouse tumor-draining lymph nodes. The results show that mature DCs were significantly higher in the STM-Mn@OMVs, Mixture, and OMVs group compared to the other groups (Fig. 2A). It is well established that CD80 and CD86 are two crucial co-stimulatory molecules predominantly expressed on DCs, which are instrumental in antigen presentation and T cell activation[35]. CD80 and CD86 bind to CD28 molecules on T cells and provide co-stimulatory signals that contribute to T cell activation, proliferation, and differentiation. They are also involved in the proliferation of regulatory T cells (Tregs) and thus play an important role in immunomodulation[36]. Among the single-component groups,

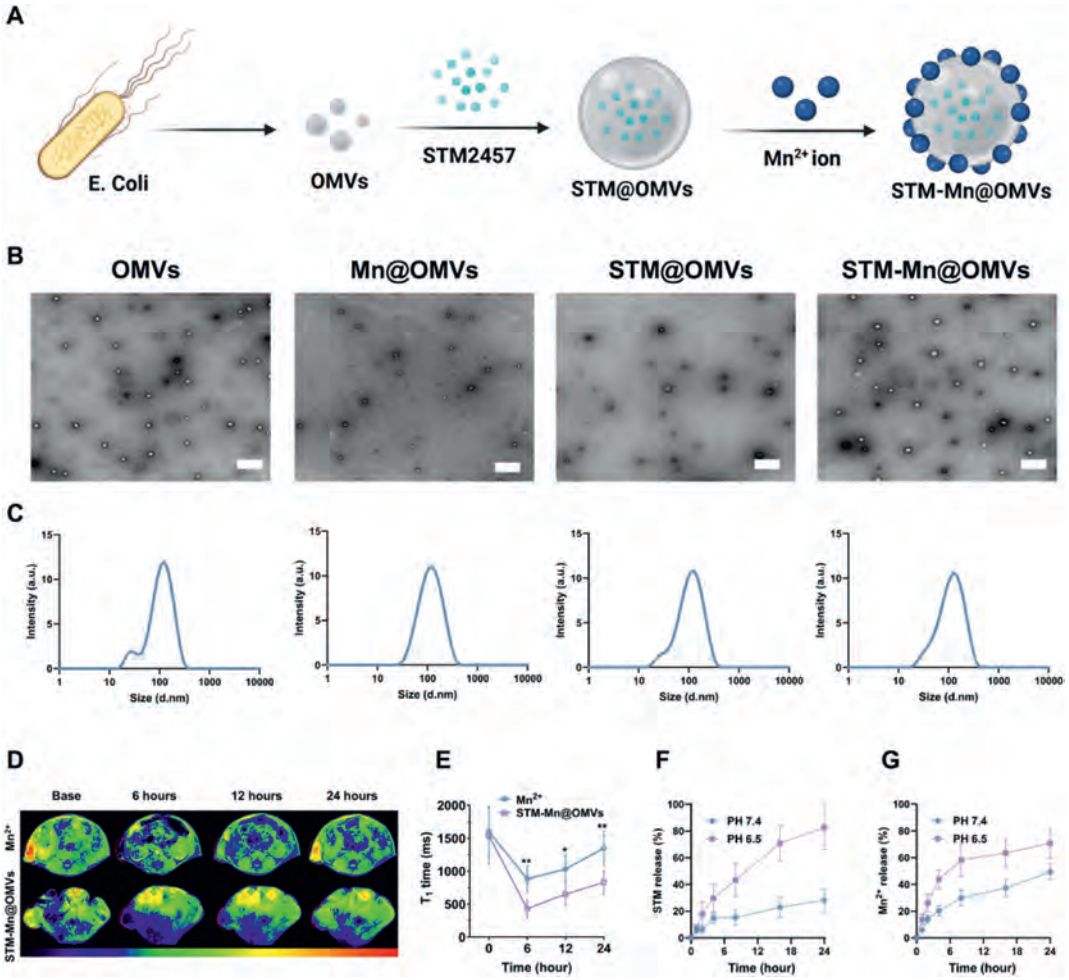

Figure 1 Structural and MRI characterization of STM-Mn@OMVs. (A) Schematic diagram of the synthesis of STM-Mn@OMVs. This figure was created in BioRender. Jiaxin, Y. (2025) https://BioRender.com/m32y910. (B) TEM image of OMVs, STM@OMVs, Mn@OMVs, and STM-Mn@OMVs. Scale bar = 300 nm. (C) The average diameter image of OMVs, STM@OMVs, Mn@OMVs, and STM-Mn@OMVs. (D) Representative T1-weighted MR images of tumor mice after treatment of STM-Mn@OMVs or free Mn^{2+} after i.t. administration for 24 h. (E) T1 relaxation time plots of Mn^{2+} signal in the tumor region after i.t. injection of STM-Mn@OMVs or free Mn^{2+} for 24 h. (F, G) Cumulative release percentage of STM2457 (F) and Mn^{2+} (G) under various pH values at different time points. $^*P < 0.05$; $^{**}P < 0.01$; $^{***}P < 0.001$; ns, not significant.

the OMVs group had the highest expression of CD80 and CD86 and the highest content of mature DCs, so we hypothesized that OMVs in STM-Mn@OMVs played an important role in promoting DCs' maturation. And the STM-Mn@OMVs group exhibited the highest expression of CD80 and CD86 in lymph nodes (42.0%), and the highest percentage of infiltrated $CD8^+CD3^+$ T-cell populations (34.8%) among all administered groups (Fig. 2B−D). This shows that the material we constructed significantly enhances DCs' maturation compared to single components and pure mixtures. Furthermore, the serum of mice in the STM-Mn@OMVs group exhibited a notable elevation in the expression of IL-12p70 (Fig. 2E), predominantly secreted by DCs and other antigen-presenting cells (APCs)[37]. Additionally, the levels of IL-1β, IL-6, and TNF-α, crucial cytokines in immune regulation and antitumor immunity, were also significantly elevated (Fig. 2F−H).

We analysed the tumor tissues of mice for STING pathway-related proteins. Compared to the other groups, the phosphorylation of STING, IRF3, and TBK1 was increased in the Mn, Mixture, and STM-Mn@OMVs groups (Fig. 2I), most significantly in the STM-Mn@OMVs group. This suggests that STM-Mn@OMVs plays a role in the STING/TBK1/IRF3 innate immune pathway. The aforementioned results demonstrate that the designed materials, STM-Mn@OMVs, are capable of stimulating the immune system by promoting DCs maturation, antigen presentation, and T cell activation to a greater extent than single components and mixtures (Fig. 2J). Furthermore, STM-Mn@OMVs were observed to more effectively activate STING pathways, promote immune cell infiltration, and enhance antitumor immunity. This provides a reliable basis for the selection of materials for our study and validates the feasibility of subsequent studies.

3.2. STM-Mn@OMVs significantly inhibited tumor growth in the in vivo study

To confirm whether STM-Mn@OMVs has a tumor growth inhibitory effect, the Hepa1-6 hepatocellular carcinoma mouse

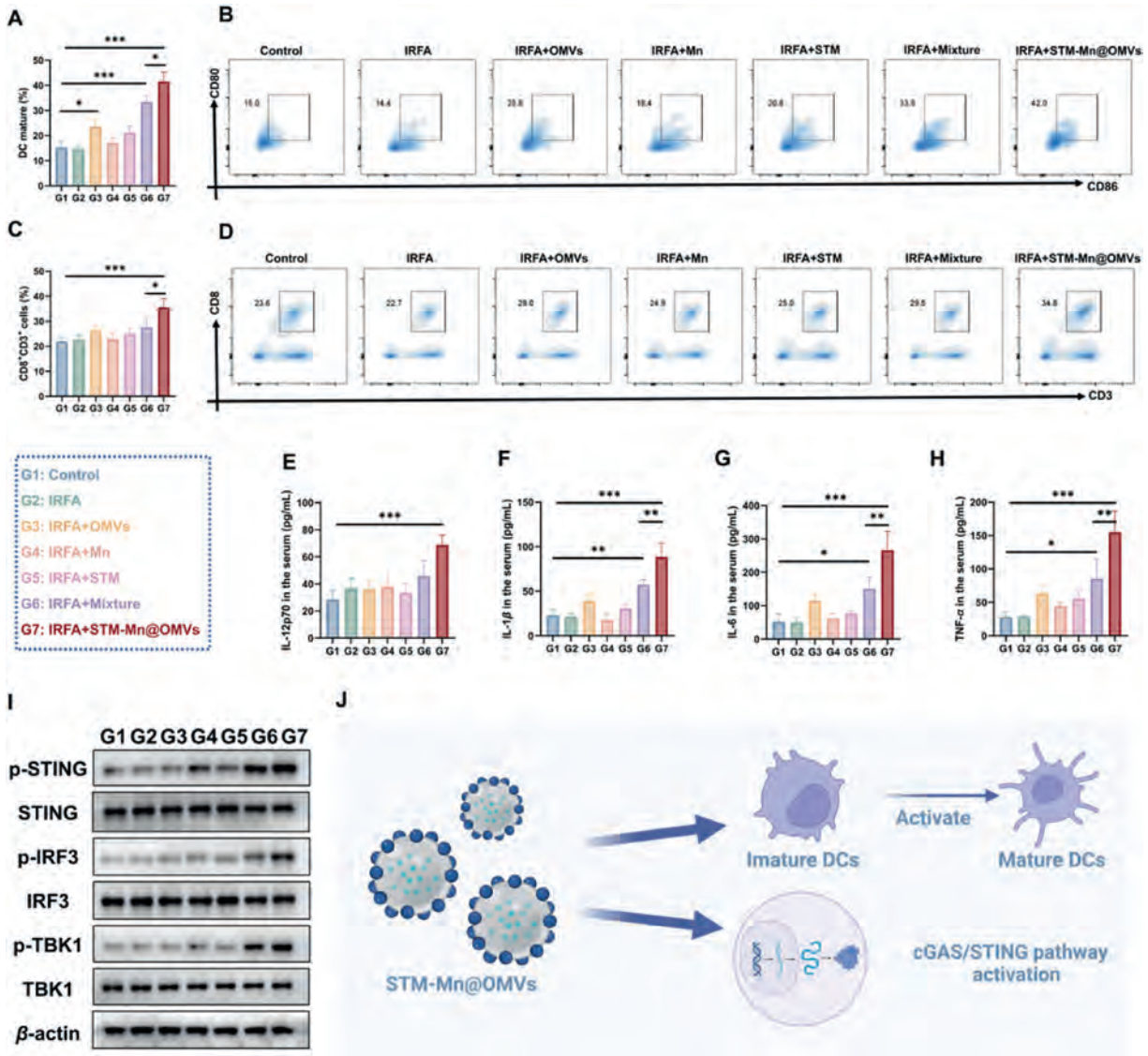

Figure 2 STM-Mn@OMVs activate immune and STING pathways. (A) Histogram of maturation of DCs for different treatments. (B) Flow cytometry scatter plots of $CD80^+CD86^+$ T cells in the mouse tumor tissue following different treatments. (C) Flow cytometry histograms of $CD8^+CD3^+$ T cells in the tumor tissue following different treatments. (D) Flow cytometry scatter plots of $CD8^+CD3^+$ T cells in the mouse tumor tissue following different treatments. (E−H) Histograms of IL-12p70 (E), IL-1β (F), IL-6 (G), and TNF-α (H) expression levels in mouse serum after different treatments. (I) WB analysis will be used to assess the levels of p-STING, STING, p-IRF3, IRF3, p-TBK1, and TBK1 expression in the tumor tissues of mice subjected to different treatments. (J) Schematic of STM-Mn@OMVs promoting DCs maturation and activation of the cGAS/STING pathway. This figure was created in BioRender. Jiaxin, Y. (2025) https://BioRender.com/c70z871. Data are presented as mean ± SD ($n = 3$). *$P < 0.05$; **$P < 0.01$; ***$P < 0.001$; ns, not significant.

model was cultured for seven days following a subcutaneous inoculation. Once the tumors had reached approximately 150 mm^3, the mice were randomly divided into six groups. Five of these groups were pre-treated with IRFA, while one group served as the control group and was not pre-treated with IRFA (Fig. 3A). The results of IRFA following the treatment of mice in each group with different drugs demonstrated that mice treated with Mn@OMVs, STM@OMVs, and STM-Mn@OMVs exhibited a notable delay in tumor growth (Fig. 3B−G). The combination of STM2457 and Mn^{2+} exerted a synergistic effect, resulting in a notable reduction in tumor size and weight in the STM-Mn@OMVs group (Fig. 3H and I, Supporting Information Fig. S4), which indicated that the STM-Mn@OMVs treatment regimen exhibited the most pronounced antitumor efficacy. The results demonstrate a correlation between tumor size and survival rate in mice. In the control group, all mice succumbed to the disease within 25 days. In contrast, the mice treated with STM-Mn@OMVs exhibited the highest survival rate, with 40% of mice surviving for at least 60 days (Fig. 3J). No significant weight loss was observed in any of the treatment groups during the 14-day observation period (Fig. 3K), which preliminarily suggests that STM-Mn@OMVs have a favourable biosafety profile.

To further verify the antitumor effect of STM-Mn@OMVs from histological and cellular molecular perspectives, tumor tissues were collected for H&E, Ki-67, and TUNEL staining, as well as Western blot analysis, 14 days after treatment in mice. In

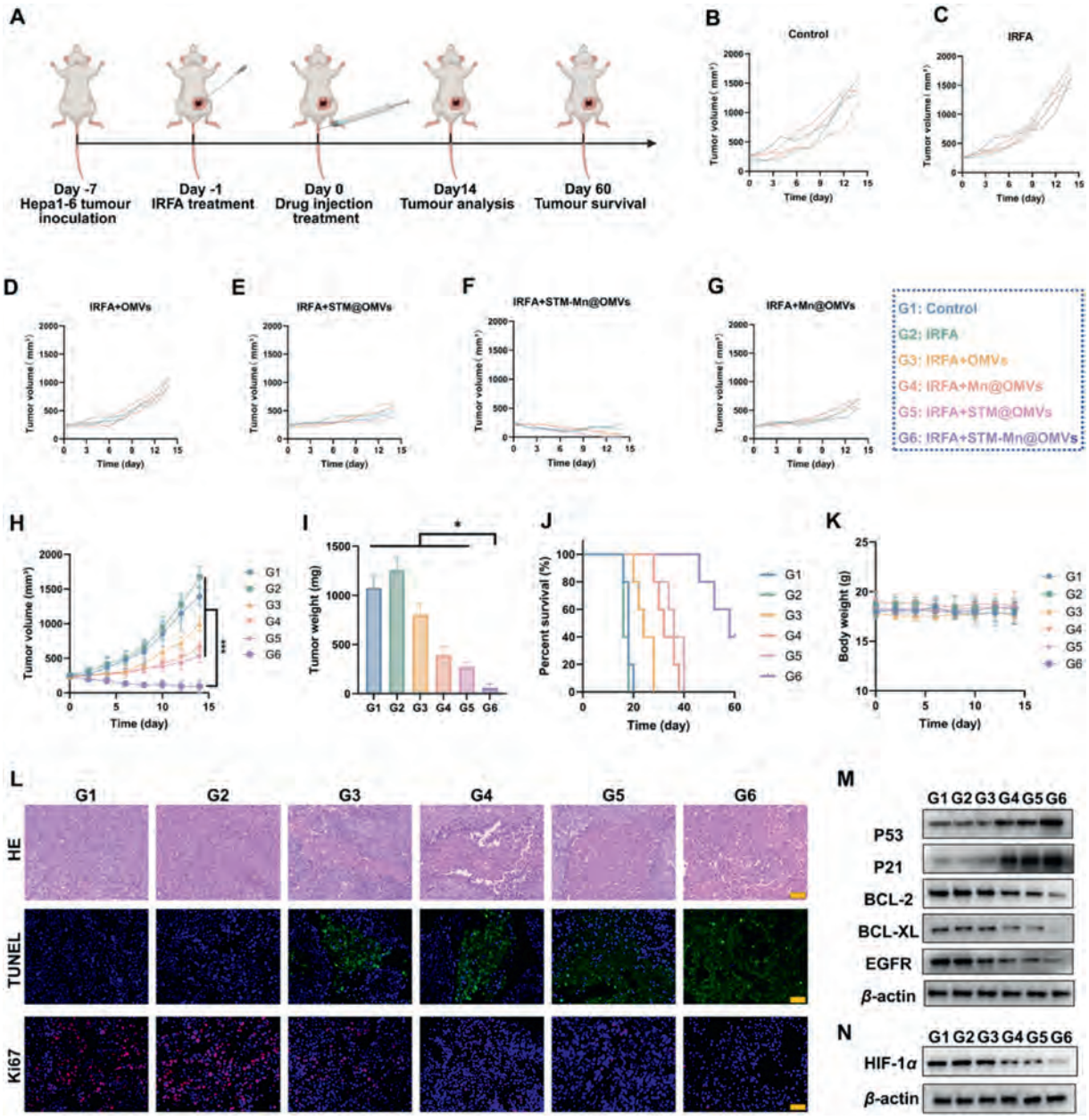

Figure 3 STM-Mn@OMVs significantly inhibited the subcutaneous tumor development. (A) Schematic diagram of treatment protocols. This figure was created in BioRender. Jiaxin, Y. (2025) https://BioRender.com/gr91chf. (B−H) Individual (B−G) and average (H) tumor growth kinetics of various treatment groups, starting from treatment Day 0, and the average body weight of mice in each group are shown. (I) Tumor weights on Day 14 after different treatment groups are displayed. (J) Survival curves of different treated mice. (K) Body weights on Day 14 after different treatment groups are displayed. (L) H&E, Ki-67, and TUNEL immunostained images for Hepa1-6 tumor tissues on Day 14 of different treatments. Scale bar = 50 μm. (M) WB analysis will be used to assess the levels of P53, P21, BCL-2, BCL-XL and EGFR expression in the tumor tissues of mice subjected to different treatments. (N) WB analysis will be used to assess the levels of HIF-1α expression in the tumor tissues of mice subjected to different treatments. Data are presented as mean ± SD ($n = 5$). *$P < 0.05$; **$P < 0.01$; ***$P < 0.001$; ns, not significant.

comparison to the other control groups, the mice in the STM-Mn@OMVs group exhibited markedly reduced levels of H&E and Ki67 staining, thereby providing compelling evidence that the drug effectively inhibited tumor proliferation (Fig. 3L and Supporting Information Fig. S5). The results of the TUNEL assay demonstrated that the intensity of green fluorescence of the indicated DNA fragments (Fig. 3L and Fig. S5) was significantly elevated in the STM-Mn@OMVs group in comparison to the other groups. This observation suggests that STM-Mn@OMVs-treated tumor tissues have a higher level of DNA damage, confirming that it can significantly promote cancer cell apoptosis. Western blot analysis demonstrated that the STM-Mn@OMVs group inhibited tumor proliferation and promoted the up-regulation of apoptosis-promoting proteins P53 and P21 (Fig. 3M). In contrast, the anti-apoptotic proteins BCL-2 and BCL-XL, which inhibit apoptosis and support tumor cell survival,

were down-regulated (Fig. 3M). Additionally, the expression levels of epidermal growth factor receptor (EGFR) and hypoxia-inducible factor 1 alpha (HIF-1α), both of which promote tumor angiogenesis, were also reduced (Fig. 3N). In conclusion, the data demonstrate that STM-Mn@OMVs effectively inhibit cancer cell proliferation and stimulate apoptosis *in vivo*, indicating their crucial role in tumor growth inhibition.

3.3. STM-Mn@OMVs promotes tumor cells' pyroptosis

To further investigate the mechanism by which STM-Mn@OMVs promote antitumor immunity, tumor tissues were taken for flow cytometry analysis and Western blot staining seven days after drug administration in the mouse model (Fig. 4A). The gating and sorting strategy used in flow cytometry analysis is detailed in the Supporting Information (Supporting Information Figs. S6−S9). Firstly, the activation of T cells and natural killer (NK) cells was analysed by flow cytometry, which demonstrated a considerable increase in the proportion of $CD45^+$ T cells infiltrating tumor tissues in the STM-Mn@OMVs group (Fig. 4B and E). Additionally, there was a notable rise in the number of $CD8^+CD3^+$ T cells and activated $CD8^+$ T cells, including those expressing IFNγ^+, GZMB$^+$, TNF-α^+, and Ki67$^+$ (Fig. 4C, F, and H−K, Supporting Information Figs. S10−S13). The proportion of NK cells ($CD3^+NK1.1^+$) was also significantly increased at 7.85% (Fig. 4D and G), and the immunofluorescence showed significantly increased CD8 and NKp46 immunofluorescence in the STM-Mn@OMVs group (Supporting Information Figs. S14 and S15). The observed increase in these markers indicated that $CD8^+$ T cells and NK cells were effectively activated, and that activated $CD8^+$ T cells and NK cells were able to recognise and kill tumor cells more effectively. In antitumor immunity, CTLs as well as NK cells are important for tumor control and clearance[38,39].

In our designed STM-Mn@OMVs material, both Mn^{2+} and OMVs have been reported to induce the onset of cellular pyroptosis[23,40], which can further promote T-cell activation[41]. Western blot staining for cellular pyroptosis-related proteins was then performed, which demonstrated a reduction in the expression of pro-Caspase-1 and Gasdermin-D (GSDMD) and an increase in the expression of NLRP3, GSDMD-N-terminal domain (GSDMD-N), cleaved-activated Caspase-1, and IL-1β in tumor tissues treated with STM-Mn@OMVs (Fig. 4M and N). Flow cytometry analysis showed that IL-1β was also significantly increased in STM-Mn@OMVs treated tumor tissues (Fig. 4L). This finding provides compelling evidence that STM-Mn@OMVs induce cellular pyroptosis. The results demonstrate that the designed drug, STM-Mn@OMVs, can promote the formation of NLRP3, thereby facilitating the cleavage of pro-Caspase-1 into its active form, Caspase-1, to a certain extent. Caspase-1 can cleave GSDMD to generate active GSDMD-N and promote cellular pyroptosis[24]. In addition, the activated Caspase-1 promotes the active IL-1β formation, amplifying the inflammatory response[24]. To further elucidate the relationship between cellular pyroptosis and STING activation, we introduced the pyroptosis inhibitor (Disulfiram) into the G6 treatment regimen. Disulfiram, a well-documented agent, effectively prevents the formation of GSDMD membrane pores, thereby halting the process of cellular pyroptosis[42]. We employed Western blot analysis to evaluate the expression levels of proteins associated with the STING pathway and cellular pyroptosis, including p-TBK1, p-STING, p-IRF3, IL-1β, cleaved-GSDMD-N, and cleaved-Caspase-1 in the G2 (IRFA), G6 (IRFA + STM-Mn@OMVs), and G6+Disulfiram groups. Our results indicate that the combined administration of STM-Mn@2457 and Disulfiram can significantly down-regulate the expression of STING protein and the levels of pyroptosis-related proteins (Supporting Information Fig. S16). To further investigate whether the Caspase-3/GSDME axis was concurrently activated and contributed to cellular pyroptosis induction, we performed Western blot analysis to assess the expression levels of relevant proteins in tumor tissues from mice in groups G1 to G6, including pro-Caspase-3, cleaved-Caspase-3, GSDME, and cleaved GSDME-N. Our results demonstrated that the pyroptosis induced by STM-Mn@OMVs did not occur *via* the Caspase-3/GSDME signaling pathway (Supporting Information Fig. S17). These findings confirm that inhibiting cellular pyroptosis effectively reduces STING activation, thus shedding light on the intimate correlation between Caspase-1/GSDMD pyroptosis and STING pathway activation. Granzyme B (GZMB), a protease released by NK cells and $CD8^+$ T cells that induces apoptosis in target cells, is a crucial effector molecule in tumor cell killing by NK cells and CTLs[43]. Our findings revealed a markedly elevated level of GZMB immunofluorescence in tumor tissues treated with the STM-Mn@OMVs group (Supporting Information Fig. S18). These observations indicate that STM-Mn@OMVs can effectively stimulate the immune system and correlate with cellular pyroptosis, which collectively contribute to the effect of robust antitumor immunity against tumor progression (Fig. 4O).

3.4. STM-Mn@OMVs reverse immunosuppression of immunomodulatory properties

As residual tumor cells after IRFA are able to induce infiltration of MDSCs and TAMs, they accelerate residual tumor progression[11,12]. To investigate whether STM-Mn@OMVs could reduce the infiltration of suppressor immune cells and reverse the immune-suppressive tumor microenvironment, we analysed the infiltration of relevant immune cells in mice seven days after drug administration by flow cytometry analysis (Fig. 4A). The results show that the proportions of Tregs ($CD25^+Foxp3^+$ T cells) (Fig. 5A and E) and MDSCs ($CD11b^+Gr\text{-}1^+$ T cells) (Fig. 5B and F) in the STM-Mn@OMVs group were significantly lower compared to the other groups. This suggests that STM-Mn@OMVs treatment effectively suppressed the expression of Tregs and MDSCs. In addition, we analysed macrophages within the tumor microenvironment (TME) to gain insight into the immunomodulatory role played by STM-Mn@OMVs. Compared to the other groups, the STM-Mn@OMVs treatment group showed a significant increase in $CD86^+F4/80^+$ M1 macrophages (Fig. 5C and G), a decrease in $CD206^+F4/80^+$ M2 macrophages (Fig. 5D and H), and the highest M1/M2 ratio (Fig. 5I). In the tumor microenvironment, M1-type macrophages play an active role in antitumor immunity by helping to activate T cells and NK cells and promoting immune responses[44]. In contrast, M2-type macrophages play a pro-tumor role in tumor progression, accelerating tumor development by promoting angiogenesis and supporting tumor cell invasion and metastasis[44]. Our results indicated that STM-Mn@OMVs drugs enhance the antitumor activity of M1 macrophages while simultaneously impeding the pro-tumor function of M2 macrophages, ultimately leading to the inhibition of tumor progression. Furthermore, flow cytometry analysis demonstrated that the expression levels of antitumor and proinflammatory cytokines were elevated in the tumor tissues of the STM-Mn@OMVs group, including IL-2, IL-6, IL-12p70, IFN-γ,

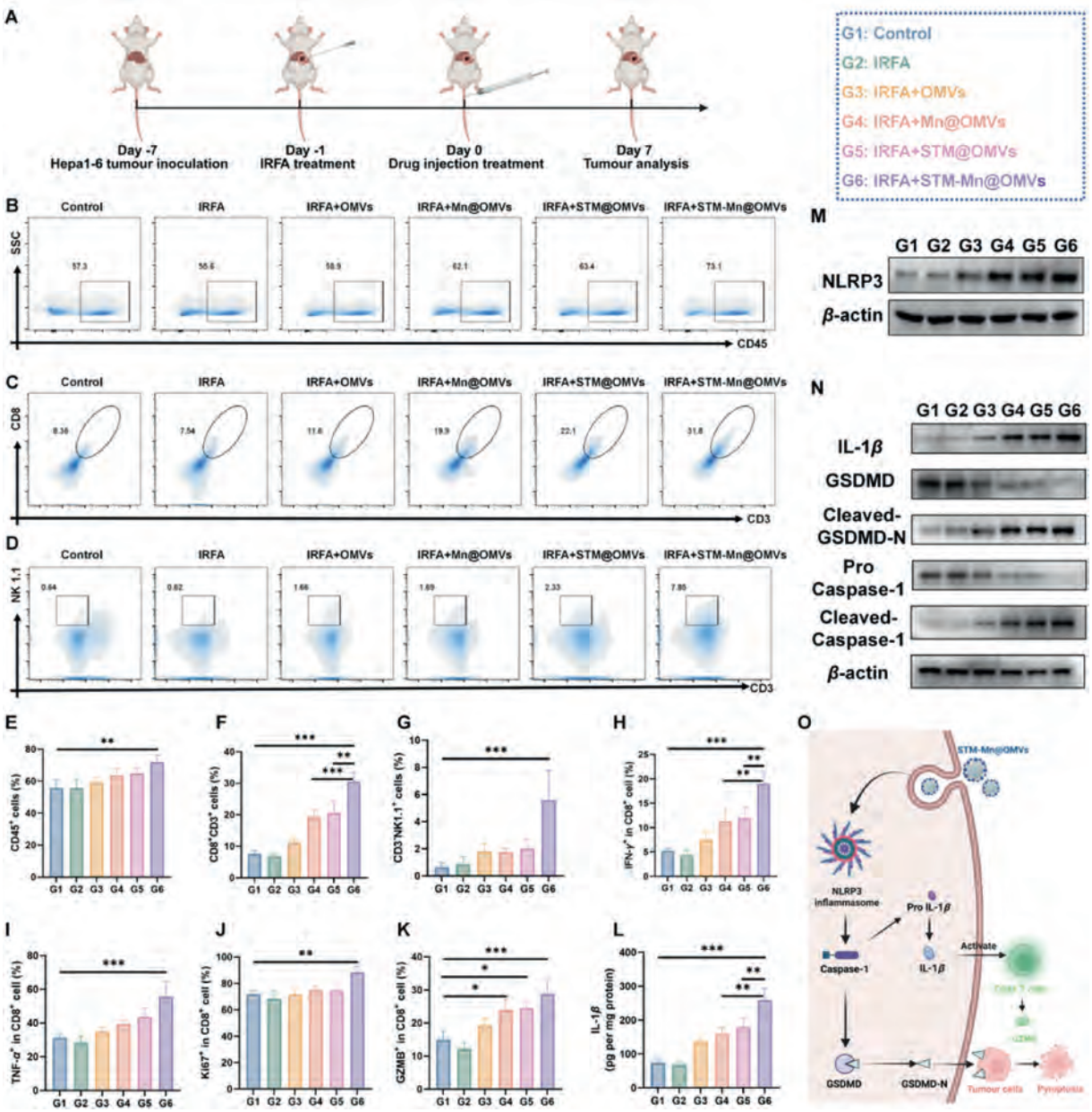

Figure 4 STM-Mn@OMVs promote tumor cells' pyroptosis. (A) Schematic diagram of treatment protocols. This figure was created in BioRender. Jiaxin, Y. (2025) https://BioRender.com/1wei0xy. (B, E) Flow cytometry scatter plots and flow cytometry histograms of $CD45^+$ T cells in the mouse tumor tissue following different treatments. (C, F) Flow cytometry scatter plots and flow cytometry histograms of $CD8^+CD3^+$ T cells in the mouse tumor tissue following different treatments. (D, G) Flow cytometry scatter plots and flow cytometry histograms of $CD3^+NK1.1^+$ T cells in the mouse tumor tissue following different treatments. (H−K) Flow cytometry scatter plots of $IFN\gamma^+CD8^+$ (H), $TNF\text{-}\alpha^+CD8^+$ (I), $Ki67^+CD8^+$ (J), and $GZMB^+CD8^+$ (K) T cells in the mouse tumor tissue following different treatments. (L) The level of IL-2 expression was determined by ELISA in tumor tissues on Day 7 of different treatments. (M) WB analysis will be used to assess the levels of NLRP3 expression in the tumor tissues of mice subjected to different treatments. (N) WB analysis will be used to assess the levels of IL-1β, GSDMD, cleaved-GADMD-N, pro-Caspase-1, and cleaved-Caspase-1 expression in the tumor tissues of mice subjected to different treatments. (O) Schematic of STM-Mn@OMVs promoting tumor cells' pyroptosis. This figure was created in BioRender. Jiaxin, Y. (2025) https://BioRender.com/lmsusjg. Data are presented as mean ± SD ($n = 3$). $^*P < 0.05$; $^{**}P < 0.01$; $^{***}P < 0.001$; ns, not significant.

and IFN-β. Conversely, the levels of inhibitory cytokines, particularly TGF-β and IL-10, were markedly reduced (Fig. 5J−P).

The aforementioned findings indicate that STM-Mn@OMVs are capable of reducing the infiltration of immunosuppressive cell populations, including Tregs and MDSCs. Conversely, they facilitate an increase in the M1 macrophage phenotype within the TAM, which results in a shift from an immunosuppressive to an immune-responsive macrophage phenotype. Furthermore, STM-

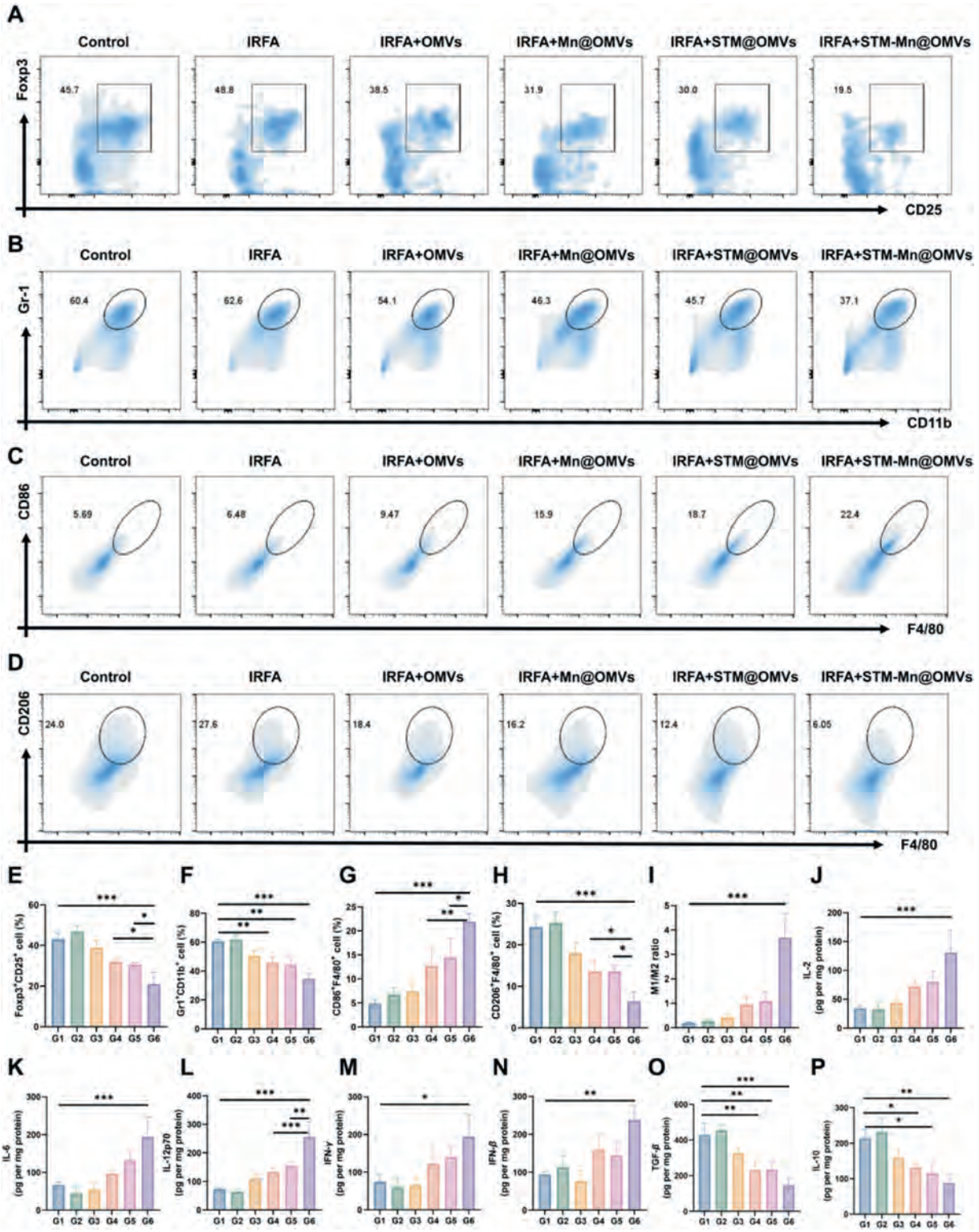

Figure 5 STM-Mn@OMVs reverse immune-suppressive tumor microenvironment. (A, E) Flow cytometry scatter plots and flow cytometry histograms of $CD25^+Foxp3^+$ T cells in the mouse tumor tissue following different treatments. (B, F) Flow cytometry scatter plots and flow cytometry histograms of $CD11b^+Gr\text{-}1^+$ T cells in the mouse tumor tissue following different treatments. (C, G) Flow cytometry scatter plots and flow cytometry histograms of $CD86^+F4/80^+$ M1 macrophages in the mouse tumor tissue following different treatments. (D, H) Flow cytometry scatter plots and flow cytometry histograms of $CD206^+F4/80^+$ M2 macrophages in the mouse tumor tissue following different treatments. (I) Flow cytometry histograms of the M1/M2 ratio in the mouse tumor tissue following different treatments. (J–P) The level of IL-2 (J), IL-6 (K), IL-12p70 (L), IFN-γ (M), IFN-β (N), TGF-β (O), and IL-10 (P) expression was determined by ELISA in tumor tissues. Data are presented as mean ± SD ($n = 3$). *$P < 0.05$; **$P < 0.01$; ***$P < 0.001$; ns, not significant. G1, Control group; G2, IRFA group; G3, IRFA + OMVs group; G4, IRFA + Mn@OMVs group; G5, IRFA + STM@OMVs; G6, IRFA + STM-Mn@OMVs.

Mn@OMVs were observed to reverse the inhibitory TIME by reducing the expression of inhibitory cytokines and promoting the expression of antitumor cytokines. The aforementioned evidence substantiates the assertion that STM-Mn@OMVs exert a pivotal influence on the efficacy of immunotherapy.

3.5. Assessment of immune activation and therapeutic efficacy in the orthotopic mouse model of HCC

To further verify whether the proposed STM-Mn@OMVs have tumor growth inhibitory effects in an orthotopic tumor model, we used a Hepa1-6 mouse in an orthotopic hepatocellular carcinoma model for our experiments. The mice were randomly divided into two groups after the tumors had grown to approximately 150 mm^3, and one group was injected with PBS after IRFA pretreatment, and the other group was injected with STM@OMVs (Fig. 6A). Tumor growth was meticulously monitored through the assessment of bioluminescent signals, as the intensity of these signals is directly proportional to tumor volume (Fig. 6B). The statistical analysis of the relative fluorescence signals in different treatment groups is shown in Supporting Information Fig. S19. The gross morphological images and histopathological sections of tumors following treatment in the orthotopic liver cancer model are presented in Supporting Information Figs. S20 and S21. These findings revealed that mice treated with STM-Mn@OMVs exhibited a notable delay in tumor growth or even complete regression. The survival rate of mice in the IRFA group was less than 20 days, whereas 40% of mice in the STM-Mn@OMVs group survived for at least 80 days (Fig. 6C). Tumor tissues were collected for H&E, Ki-67, and TUNEL staining, as well as Western blot analysis, 7 days after the treatment in mice. In comparison to the IRFA group, the mice in the STM-Mn@OMVs group exhibited markedly

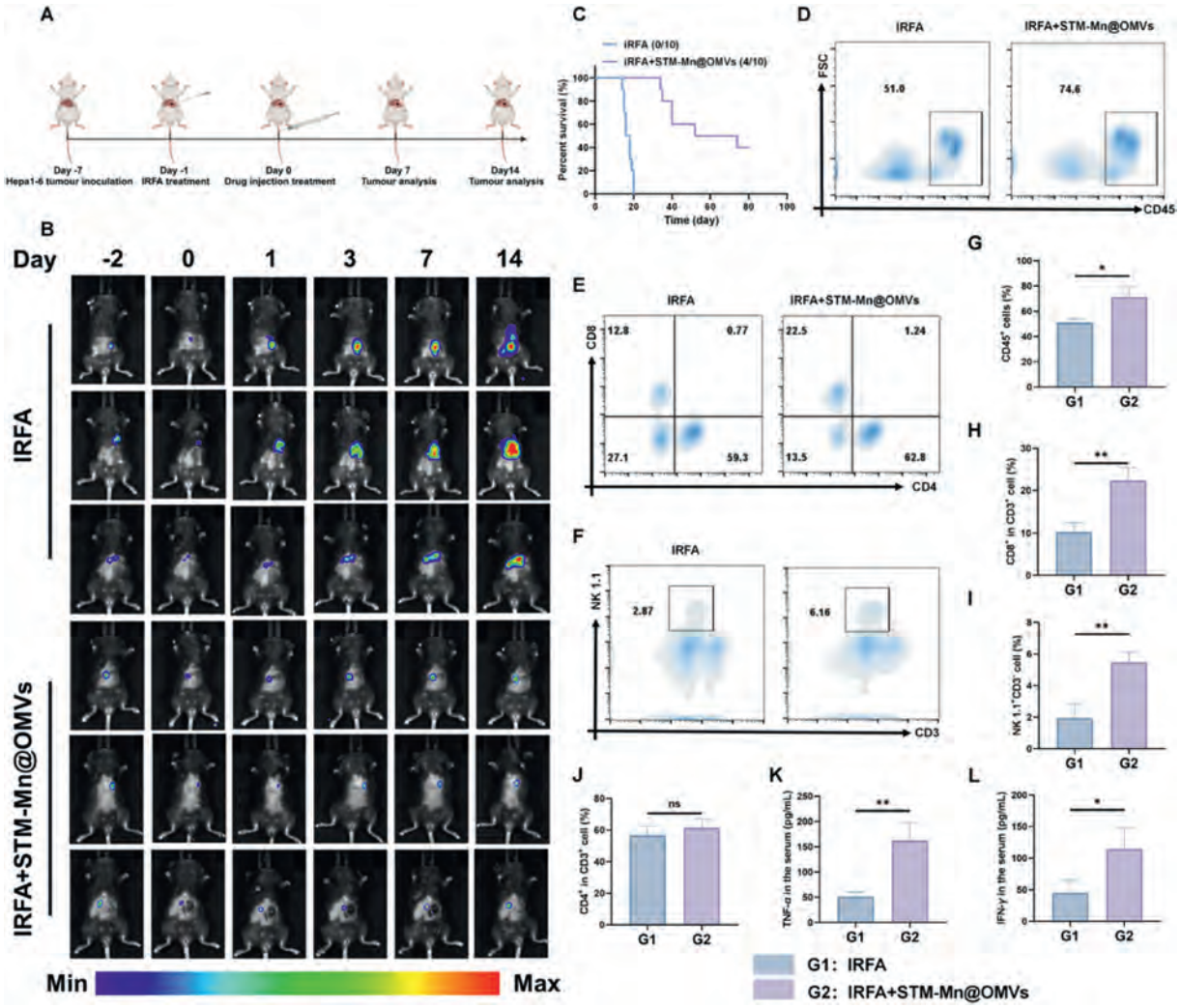

Figure 6 The immune activation and therapeutic efficacy of STM-Mn@OMVs in orthotopic HCC mice. (A) Schematic diagram of treatment protocols. This figure was created in BioRender. Jiaxin, Y. (2025) https://BioRender.com/b03u398. (B) Bioluminescence images of HCC tumor mice after different treatments within 14 days of observation. (C) Survival curves of different treated mice (living mice/dead mice). (D−F) Flow cytometry scatter plots of CD45$^+$ T cells (D), CD4$^+$CD8$^+$ T cells (E), and NK cells (CD3$^+$NK1.1$^+$) (F) in the mouse tumor tissue following different treatments. (G−J) Flow cytometry histograms of CD45$^+$ T cells (G), CD8$^+$CD3$^+$ T cells (H), NK cells (NK1.1$^+$CD3$^+$) (I), and CD4$^+$CD3$^+$ T cells (J) in the mouse tumor tissue following different treatments. (K, L) Histograms of TNF-α (K) and IFN-γ (L) expression levels in mouse serum after different treatments. Data are presented as mean ± SD ($n = 5$). *$P < 0.05$; **$P < 0.01$; ***$P < 0.001$; ns, not significant.

reduced levels of H&E and Ki67 staining, thereby substantiating the efficacy of the drug in inhibiting tumor proliferation (Supporting Information Fig. S22). The TUNEL staining yielded the same result as before, namely that the STM-Mn@OMVs group exhibited a higher green fluorescence intensity than the IRFA group (Fig. S22). This observation corroborates the hypothesis that STM-Mn@OMVs-treated in orthotopic tumors also have higher levels of DNA damage, thereby confirming its ability to significantly promote cancer cell apoptosis.

To further elucidate the alterations in key enzymes associated with the m^6A RNA methylation process following IRFA treatment, we established a mouse orthotopic HCC model and employed Western blot analysis to assess the expression levels of critical components involved in the m^6A RNA methylation pathway in tumor tissues from both control mice (not subjected to IRFA) and IRFA-treated mice. The results demonstrate that the expression levels of METTL3, METTL14, YTHDF1, PD-L1, and EGFR were significantly increased after IRFA treatment (Supporting Information Fig. S23). In contrast, no significant changes were detected in the expression of WTAP, FTO, ALKBH5, or YTHDF2. Subsequently, we evaluated the expression levels of METTL3, METTL14, YTHDF1, EGFR, and PD-L1 in HCC cells following treatment with IRFA + PBS and IRFA + STM-Mn@OMVs using Western blot analysis. The results demonstrate that the protein levels of METTL3, METTL14, YTHDF1, and EGFR were significantly reduced in tumor cells from mice treated with IRFA + STM-Mn@OMVs, and PD-L1 expression was also correspondingly decreased (Supporting Information Fig. S24). This demonstrates that STM-Mn@OMVs can inhibit the functions of m^6A methylation modification-related enzymes, such as METTL3, METTL14, and YTHDF1, and suppress the activation of the YTHDF1−EGFR axis. Following seven days of treatment in mice, tumor tissue and blood samples were collected for flow cytometry analysis. The results of the analysis of tumor tissue samples demonstrated that STM-Mn@OMVs exhibited a significantly higher degree of infiltration into $CD45^+$ T cells, $CD4^+CD8^+$ T cells, NK cells ($CD3^+NK1.1^+$), and $CD8^+CD3^+$ T cells compared to the IRFA group (Fig. 6D−I). Conversely, no notable difference was observed in the proportion of $CD3^+CD4^+$ T cells (Fig. 6J). This verified that $CD8^+$ T and NK cells were also effectively activated in the orthotopic hepatocellular carcinoma model, thereby exerting antitumor effects. Furthermore, the results of flow analysis of serum demonstrated that the levels of TNF-α and IFN-γ were markedly elevated in the STM-Mn@OMVs group in comparison to the IRFA group (Fig. 6K and L). The aforementioned evidence substantiates the assertion that STM-Mn@OMVs is capable of enhancing antitumor immunity and inhibiting tumor growth in the orthotopic model of mouse hepatocellular carcinoma.

3.6. Biocompatibility and toxicity studies of STM-Mn@OMVs

In our study, we evaluated biochemical parameters after tail vein injection of STM-Mn@OMVs and examined histopathological changes to investigate their biocompatibility and potential adverse effects. As shown in Supporting Information Fig. S25, STM-Mn@OMVs treatment did not induce any significant pathological changes in major organs such as the heart, lung, liver, spleen, and kidney. In addition, biochemical indices of liver and kidney function (ALT, AST, ALB, CREA, UREA, γ-GT, CK, and LDH) were within acceptable limits (Supporting Information Figs. S26 and S27). In addition, the body weight of the mice remained stable throughout the treatment period. To further investigate the biodistribution of STM-Mn@OMVs, we analyzed Mn^{2+} levels at various time points post-injection in both subcutaneous and orthotopic HCC models using ICP-OES. The results reveal that STM-Mn@OMVs predominantly accumulated in the liver and tumor tissues across both models, with minimal deposition in the heart, spleen, lungs, and kidneys (Supporting Information Figs. S28 and S29). Notably, in the orthotopic HCC model, STM-Mn@OMVs exhibited enhanced liver- and tumor-specific targeting, accompanied by a marked reduction in off-target accumulation. Collectively, these findings demonstrate that the STM-Mn@OMVs we developed exhibit favorable liver/tumor-targeting capabilities and do not induce acute hepatic or renal toxicity or any observable systemic toxicity during the treatment period. These observations support the conclusion that STM-Mn@OMVs possess excellent targeting specificity and biosafety, highlighting their promising potential for clinical application in reducing the risk of tumor recurrence following IRFA in HCC.

4. Discussion

In hepatocellular carcinoma (HCC), insufficient radiofrequency ablation (IRFA) leads to a significant increase in the m^6A methylation modification level in HCC tumor cells, with the expression of YTHDF1 (as an m^6A recognition protein) being significantly upregulated, thereby promoting the expression of EGFR and further exacerbating the recurrence and progression of HCC after IRFA[7]. Additionally, during this process, the m^6A methyltransferase METTL3 undergoes nuclear translocation, further enhancing its catalytic activity. Moreover, a recent study showed that IRFA promotes residual HCC growth and leads to the formation of an immune-suppressive tumor microenvironment[45]. Therefore, reducing m^6A RNA methylation levels after RFA treatment and attenuating the inhibitory immune microenvironment that promotes tumor growth can effectively reduce residual tumor recurrence due to IRFA. Based on this, the STM-Mn@OMVs (a nano-carrier functionalized by rationally loading Mn^{2+} ions and the methylation inhibitor STM2457 onto OMVs derived from bacteria) constructed in this study were confirmed to significantly enhance the antitumor immune response and actively regulate the TIME. We found that STM-Mn@OMVs can specifically accumulate in tumor regions, possess pH-responsive therapeutic substance release characteristics, and enhance the T1-weighted signal of MRI. Moreover, STM-Mn@OMVs can down-regulate the expression of m^6A methylation modification-related enzymes while activating the innate immune system and the STING pathway. Besides, STM-Mn@OMVs were able to induce cellular pyroptosis, which further promoted the activation of the STING pathway and reversed the immune-suppressive tumor microenvironment. This ultimately led to the maximization of the clinical efficacy of RFA and the achievement of the "one plus one greater than two" effect. Therefore, we believe that this adjuvant we have designed offers new ideas and strategies for the treatment of HCC and has the potential for broad clinical application.

IRFA has been shown to promote residual HCC growth, which is characterised by a reduction in DCs infiltration within the tumor, a reduction in T-cell infiltration, a reduction in the number of cytotoxic T-cells, and an M2-type polarisation of macrophages[45,46]. In addition, the increase in tumor-infiltrating MDSCs and the decrease in T-cell-mediated antitumor immunity after RFA

may accelerate residual tumor progression[11,47]. Therefore, altering these conditions may help to inhibit residual tumor growth after IRFA. DCs are known to play an important role in antigen presentation and immunomodulation in organismal activities. As the most important antigen-presenting cells of the immune system, mature DCs are able to capture, process, and present antigens to T cells, thereby activating the T-cell killing response against tumors[48]. In antitumor therapy, promoting the maturation of DCs is a key step in enhancing the immune response and improving antitumor effects. The results demonstrate that the content of mature DCs in the lymph nodes of mice in the STM-Mn@OMVs group was markedly elevated, accompanied by elevated expression levels of CD80 and CD86 and increased infiltration of $CD8^+CD3^+$ T-cell populations. Furthermore, the expression of IL-12p70, predominantly produced by DCs and other APCs, as well as cytokines instrumental in immunomodulation and antitumor immune response (IL-1β, IL-6, TNF-α), was markedly elevated in the serum of mice in the STM-Mn@OMVs group. STING is a pivotal receptor that bridges intrinsic and adaptive immunity. It can be stimulated by heat-induced DNA damage, which in turn triggers an immune response[49]. Heat treatment has been demonstrated to induce double-stranded DNA (dsDNA) damage, a process detected by cyclic GMPAMP synthase (cGAS), which activates the interferon STING signalling pathway[49]. While activation of the cGAS/STING pathway upregulates the expression of IFN-β and other inflammatory cytokines to promote antigen presentation, maturation of DCs, and activation of $CD8^+$ T cells, which enhances the antitumor immune response and thus effectively inhibits tumor growth and metastasis[11,50,51]. We found that the phosphorylation levels of STING, IRF3, and TBK1 in the tumor tissues of IRFA-treated mice treated with STM-Mn@OMVs drugs were significantly higher and superior to those of the Mn^{2+} group, the Mn@OMVs group, and the mixture group. Mn^{2+} ions, a component of the STM-Mn@OMVs under research, have been demonstrated to augment the sensitivity and enzymatic activity of cGAS in response to dsDNA, thereby enabling cGAS to produce the secondary messenger cGAMP at low concentrations of dsDNA[52]. In addition, Mn^{2+} enhances STING activity by increasing the affinity of cGAMP-STING binding[52]. Thus, we speculate that the significant activation of the STING pathway by STM-Mn@OMVs promotes the maturation of DCs and enhances the STING pathway activation effect of Mn^{2+} due to the binding of the methylation inhibitor STM2457 to OMVs. Besides, IRFA hyperthermia treatment also activated the cGAS/STING pathway to a certain extent by inducing double-stranded DNA damage. This suggests a potential advantage of this adjuvant in promoting immune activation, enhancing antitumor immunity, and inhibiting tumor progression after IRFA treatment for hepatocellular carcinoma.

Our results demonstrate that STM-Mn@OMVs significantly inhibited tumor growth, prolonged mouse survival, and exhibited favorable biosafety profiles in both subcutaneous and orthotopic mouse models of HCC. In STM-Mn@OMVs-treated tumor tissues, the expression levels of key m^{6}A methylation-related proteins—including METTL3, METTL14, and YTHDF1—were markedly downregulated. Additionally, the expression of EGFR and PD-L1 was also significantly reduced. These findings confirm that STM-Mn@OMVs effectively suppress the activation of the YTHDF1−EGFR signaling axis during m^{6}A RNA methylation following IRFA treatment. Moreover, our data revealed increased DNA damage in the STM-Mn@OMVs treatment group, along with upregulation of pro-apoptotic proteins such as P53 and P21, and downregulation of anti-apoptotic proteins including BCL-2 and BCL-XL. Collectively, these observations further support the conclusion that STM-Mn@OMVs promotes tumor cellular apoptosis. We also observed a significant decrease in the expression of pro-angiogenic factors within the tumor microenvironment, particularly EGFR and HIF-1α. HIF-1α is a pivotal transcription factor for tumor cells, enabling the maintenance of metabolism and physiological functions in hypoxic conditions. Its elevated level is closely associated with several malignant processes, including tumor metastasis, angiogenesis, poor patient prognosis, and tumor resistance to drug therapy[53]. Whereas EGFR, as a receptor tyrosine kinase, is involved in cell proliferation, differentiation, and survival[54], its aberrant activation promotes tumor formation. Besides, it has been demonstrated that the interaction between EGFR and HIF-1α may influence the biological behaviour of tumors[55]. Consequently, STM-Mn@OMVs have been demonstrated to impede tumor growth and metastasis to a degree by regulating the expression of HIF-1α and EGFR.

The complementary roles of activated $CD8^+$ T cells and NK cells in antitumor immunity have been elucidated[38,39,56]. $CD8^+$ T cells recognise and kill cancer cells, while NK cells respond rapidly and directly kill those expressing stress molecules[57]. Furthermore, NK cells can facilitate the activation and proliferation of $CD8^+$ T cells through the expression of co-stimulatory receptors and cytokines, thereby forming a synergistic antitumor immune response[58]. We found a significant increase in the proportion of $CD45^+$ T cells, $CD8^+CD3^+$ T cells, activated $CD8^+$ T cells (including $IFN\gamma^+$, $GZMB^+$, TNF-α^+, $Ki67^+$), and NK cells ($CD3^+NK1.1^+$) infiltrating the tumor tissue after STM-Mn@OMVs treatment. This provides a robust foundation for effective control of residual tumor growth following IRFA. Both Mn^{2+} and OMVs have been demonstrated to induce the onset of cellular pyroptosis[23,40,59], and that pyroptosis can further promote T cell activation[41]. Consistent with previous studies, our designed drug STM-Mn@OMVs was capable of promoting the cleavage of pro-Caspase-1 to generate active Caspase-1 to a certain extent. Caspase-1, on the one hand, is able to cleave GSDMD and generate active GSDMD-N, which directly induces the onset of cellular pyroptosis[24] and activation of the STING pathway[60]. When STM-Mn@2457 was used in combination with cellular pyroptosis inhibitors, the expression levels of STING-related proteins significantly decreased. This result further indicates that there is a close association between the cellular pyroptosis pathway mediated by Caspase-1/GSDMD and the activation of the STING signaling pathway. On the other hand, Caspase-1 cleaves pro IL-1β to generate active IL-1β, thereby activating CTLs and inducing the secretion of GZMB, ultimately achieving effective killing of tumor cells[41]. In light of these findings, our study showed that the potent activation of the immune system by STM-Mn@OMVs correlates with cellular pyroptosis, which in turn promotes activation of the STING pathway. This establishes a "cyclic immunotherapy" against the tumor. This approach may also be effective against tumor progression and recurrence following IRFA.

The immune-suppressive tumor microenvironment represents a significant obstacle to the antitumor immune response, which exerts its suppressive effects on immune cell function through chemokine and cellular interactions[61]. Consequently, reversing this microenvironment can stimulate the immune system's capacity to attack tumors and improve the therapeutic efficacy. Tumor-associated macrophages (TAMs) play a complex and pivotal role in the TIME, and these macrophages can manifest either M1 or M2 characteristics. In the tumor microenvironment, M1-type macrophages exert a beneficial influence on the immune

response against tumors. This is due to their capacity to stimulate T-cell and natural killer cell (NK-cell) activation, thereby enhancing the overall immune response[44]. In contrast, M2-type macrophages could accelerate tumor progression by promoting angiogenesis and enhancing the invasiveness and metastatic ability of tumor cells[44]. The modulation of the M1/M2 balance represents a promising strategy in the context of tumor therapy. Our findings demonstrated that STM-Mn@OMVs are capable of enhancing the antitumor activity of M1 macrophages while simultaneously impeding the pro-tumor function of M2 macrophages. Furthermore, it was observed that the infiltration of immunosuppressive cell populations, such as Tregs and MDSCs, was reduced. Additionally, the expression of suppressive cytokines was found to be decreased, while the antitumor cytokines were increased. We speculate that this may be because activation of the STING pathway promotes the secretion of IFN-I (IFN-α and IFN-β), which promotes macrophage M1 polarisation[62]. In addition, activation of the STING pathway was able to inhibit MDSC expansion and T-cell suppression, and induce the production of myeloid homing chemokines in MDSCs, thereby inhibiting the immunosuppressive function of MDSCs[63]. And it also reduced the infiltration of Tregs[64], ultimately reversing the suppressive tumor immune microenvironment. The ability of STM-Mn@OMVs to reverse the suppressive immune microenvironment following antitumor immunity may help reduce the risk of tumor recurrence following IRFA.

Our results indicate that STM-Mn@OMVs, a novel adjuvant, may have potential clinical applications in the treatment of RFA in HCC. It is essential to exercise caution and closely monitor the long-term toxicity and adverse effects of its use as the clinical translation process progresses. The robust stimulation of immunity has both beneficial and adverse effects. While it enhances the capacity to eradicate tumors, it also carries the risk of triggering an exaggerated immune response within the body. Therefore, how to accurately determine the drug dose and route of administration needs to be further explored in future studies.

5. Conclusions

In conclusion, we propose a novel bio-nanocarrier for hepatocellular carcinoma RFA therapy, whereby bacterial-derived OMVs are rationally functionalised with Mn^{2+} ions and the methylation inhibitor STM2457. The STM-Mn@OMVs prepared in this study were observed to effectively promote DCs maturation, T cell activation, and the activation of STING pathways, thereby facilitating immune cell infiltration. In subcutaneously and orthotopically implanted mice models with hepatocellular carcinoma, STM-Mn@OMVs were able to significantly inhibit tumor growth and prolong the survival of the mice, suggesting their excellent therapeutic potential. Our study demonstrated that STM-Mn@OMVs can promote cellular pyroptosis and synergistically activate the STING pathway through pyroptosis, ultimately effectively activating antitumor immunity. Furthermore, STM-Mn@OMVs reduced the infiltration of immune-suppressor cell populations such as Treg cells and MDSCs and promoted the increase of M1 macrophage phenotype within the TAM, leading to the transformation of immune-suppressor macrophage phenotypes into immune-responsive phenotypes. Ultimately, the immune-suppressive tumor microenvironment was reversed to some extent. Based on the superior biosafety and therapeutic efficacy of STM-Mn@OMVs, it has significant potential for application in the field of RFA and immunotherapy for hepatocellular carcinoma.

Acknowledgments

This work was financially supported by the National Natural Science Foundation of China (Nos. 82402408 and 82271943), the Guangdong Special Support Program for Young Top-Notch Talents (No. 2024TQ08Y995, China), the Guangdong Basic and Applied Basic Research Foundation (Nos. 2023A1515012660, 2022A1515220159 and 2023A1515220128, China), the Postdoctoral Fellowship Program of CPSF (No. BX20230068, China), the China Postdoctoral Science Foundation (2024M750452), the Guangzhou Science and Technology Plan Project (No. 2023A03J1037, China), the Clinical Frontier Technology Program of the First Affiliated Hospital of Jinan University, China (No. JNU1AF-CFTP-2022-a01233) and the Nonprofit Central Research Institute Fund of the Chinese Academy of Medical Sciences (2022-RC350-04, China), the CAMS Innovation Fund for Medical Sciences (Nos. 2023-I2M-2-006 and 2023-I2M-QJ-010, China).

Author contributions

Zeyu Xiao, Kuan Hu, Duo Wang, and Liangping Luo conceived this research. Zeyu Xiao, Jiaxin Yuan, and Duo Wang synthesized the bacterial extracellular vesicles, conducted the preparation reaction, and performed structure characterization. Zeyu Xiao, Jiaxin Yuan, Qing Wu, Juan Qin, and Yiming Liu directed biological experiments and compiled the figures. Siqi Zhang, Bo Sun, Ruoxue Dai, Ni Shao, Shuang Che, Jifeng Chen, and Yin He helped to perform cell and animal experiments. Liangping Luo, Kuan Hu, Shunqian Wen, and Siqi Zhang provided critical reading and revision of the manuscript. Juan Qin, Yiming Liu, Bo Sun, Pingping Zhang, Jifeng Chen, Jiaxin Yuan, and Zeyu Xiao revised the article and supplemented the experiments. Zeyu Xiao, Jiaxin Yuan, and Qing Wu prepared the manuscript. All of the authors read and approved the manuscript.

Conflicts of interest

The authors have no conflicts of interest to declare.

Appendix A. Supporting information

Supporting information to this article can be found online at https://doi.org/10.1016/j.apsb.2025.11.005.

References

1. Marrero JA, Kulik LM, Sirlin CB, Zhu AX, Finn RS, Abecassis MM, et al. Diagnosis, staging, and management of hepatocellular carcinoma: 2018 practice guidance by the American association for the study of liver diseases. *Hepatology* 2018;**68**:723−50.
2. Vogel A, Cervantes A, Chau I, Daniele B, Llovet JM, Meyer T, et al. Hepatocellular carcinoma: ESMO clinical practice guidelines for diagnosis, treatment and follow-up. *Ann Oncol* 2018;**29**:iv238−55.
3. Guo YS, Ren YQ, Dong XJ, Kan XF, Zheng CS. An overview of hepatocellular carcinoma after insufficient radiofrequency ablation. *J Hepatocell Carcinoma* 2022;**9**:343−55.
4. Chu KF, Dupuy DE. Thermal ablation of tumours: biological mechanisms and advances in therapy. *Nat Rev Cancer* 2014;**14**:199−208.
5. Tan L, Chen SL, Wei GY, Li Y, Liao JB, Jin HL, et al. Sublethal heat treatment of hepatocellular carcinoma promotes intrahepatic metastasis and stemness in a VEGFR1-dependent manner. *Cancer Lett* 2019;**460**:29−40.

6. Home T, Jensen RA, Rao R. Heat shock factor 1 in protein homeostasis and oncogenic signal integration. *Cancer Res* 2015;**75**:907−12.
7. Su TH, Huang ML, Liao JB, Lin SB, Yu P, Yang JH, et al. Insufficient radiofrequency ablation promotes hepatocellular carcinoma metastasis through N6-methyladenosine mRNA methylation-dependent mechanism. *Hepatology* 2021;**74**:1339−56.
8. Uddin MB, Wang ZS, Yang CF. The m^{6}A RNA methylation regulates oncogenic signaling pathways driving cell malignant transformation and carcinogenesis. *Mol Cancer* 2021;**20**:61.
9. Li Q, Ni Y, Zhang LR, Jiang RQ, Xu J, Yang H, et al. HIF-1α-induced expression of m^{6}A reader YTHDF1 drives hypoxia-induced autophagy and malignancy of hepatocellular carcinoma by promoting ATG2A and ATG14 translation. *Signal Transduct Targeted Ther* 2021;**6**:76.
10. Shi LR, Wang JJ, Ding NH, Zhang Y, Zhu YB, Dong SL, et al. Inflammation induced by incomplete radiofrequency ablation accelerates tumor progression and hinders PD-1 immunotherapy. *Nat Commun* 2019;**10**:5421.
11. Wu H, Li SS, Zhou MJ, Jiang AN, He YN, Wang S, et al. Palliative radiofrequency ablation accelerates the residual tumor progression through increasing tumor-infiltrating MDSCs and reducing T-cell-mediated antitumor immune responses in animal model. *Front Oncol* 2020;**10**:1308.
12. Marvel D, Gabrilovich DI. Myeloid-derived suppressor cells in the tumor microenvironment: expect the unexpected. *J Clin Investig* 2015;**125**:3356−64.
13. Liu JY, Li XL, Li YG, Gong QY, Luo K. Metformin-based nanomedicines for reprogramming tumor immune microenvironment. *Theranostics* 2025;**15**:993−1016.
14. Song YJ, Du YF, Hu C, Lei L, Yang LY, Wang XR, et al. Metformin-mediated immunosuppressive microenvironment remodeling in combination with chemotherapy *via* a cspatial-specific multi-responsive carrier-free self-assembled nanoparticle. *Adv Funct Mater* 2024;**34**:2316145.
15. Zhang YX, Fang ZX, Pan DY, Li YK, Zhou J, Chen HY, et al. Dendritic polymer-based nanomedicines remodel the tumor stroma: improve drug penetration and enhance antitumor immune response. *Adv Mater* 2024;**36**:e2401304.
16. Wang D, Zhang L, Yang WH, Zhang LZ, Yu C, Qin J, et al. Arginine-loaded nano-calcium-phosphate-stabilized lipiodol pickering emulsions potentiates transarterial embolization-immunotherapy. *Adv Sci* 2024;**12**:e2410484.
17. Xie JH, Haesebrouck F, Van Hoecke L, Vandenbroucke RE. Bacterial extracellular vesicles: an emerging avenue to tackle diseases. *Trends Microbiol* 2023;**31**:1206−24.
18. Li M, Zhou H, Jiang W, Yang C, Miao H, Wang YC. Nanovaccines integrating endogenous antigens and pathogenic adjuvants elicit potent antitumor immunity. *Nano Today* 2020;**35**:101007.
19. Xie JH, Li QQ, Haesebrouck F, Van Hoecke L, Vandenbroucke RE. The tremendous biomedical potential of bacterial extracellular vesicles. *Trends Biotechnol* 2022;**40**:1173−94.
20. Qing S, Lyu CJ, Zhu L, Pan C, Wang S, Li F, et al. Biomineralized bacterial outer membrane vesicles potentiate safe and efficient tumor microenvironment reprogramming for anticancer therapy. *Adv Mater* 2020;**32**:e2002085.
21. Hasgur S, Fan R, Zwick DB, Fairchild RL, Valujskikh A. B cell−derived IL-1β and IL-6 drive T cell reconstitution following lymphoablation. *Am J Transplant* 2020;**20**:2740−54.
22. Kim S, Lu HC, Steelman AJ, Li JR. Myeloid Caspase-8 restricts RIPK3-dependent proinflammatory IL-1β production and CD4 T cell activation in autoimmune demyelination. *Proc Natl Acad Sci U S A* 2022;**119**:e2117636119.
23. Toldo S, Abbate A. The role of the NLRP3 inflammasome and pyroptosis in cardiovascular diseases. *Nat Rev Cardiol* 2023;**21**:219−37.
24. Rao ZP, Zhu YT, Yang P, Chen Z, Xia YQ, Qiao CQ, et al. Pyroptosis in inflammatory diseases and cancer. *Theranostics* 2022;**12**:4310−29.
25. Vande Walle L, Lamkanfi M. Pyroptosis. *Curr Biol* 2016;**26**:R568−72.
26. Wang QY, Wang YP, Ding JJ, Wang CH, Zhou XH, Gao WQ, et al. A bioorthogonal system reveals antitumour immune function of pyroptosis. *Nature* 2020;**579**:421−6.
27. Zhang ZB, Zhang Y, Xia SY, Kong Q, Li SY, Liu X, et al. Gasdermin E suppresses tumour growth by activating antitumour immunity. *Nature* 2020;**579**:415−20.
28. Wang D, Nie TQ, Huang CQ, Chen ZR, Ma XC, Fang WM, et al. Metal-cyclic dinucleotide nanomodulator-stimulated STING signaling for strengthened radioimmunotherapy of large tumors. *Small* 2022;**18**:e2203227.
29. Wang D, Deng XJ, Wang JH, Che S, Ma XC, Zhang SQ, et al. Environmentally responsive hydrogel promotes vascular normalization to enhance STING antitumor immunity. *J Control Release* 2024;**372**:403−16.
30. Wang LZ, Bi SN, Li Z, Liao AQ, Li YT, Yang LL, et al. Napabucasin deactivates STAT3 and promotes mitoxantrone-mediated cGAS−STING activation for hepatocellular carcinoma chemoimmunotherapy. *Biomaterials* 2025;**313**:122776.
31. Moore CL, Savenka AV, Basnakian AG. TUNEL assay: a powerful tool for kidney injury evaluation. *Int J Mol Sci* 2021;**22**:412.
32. Kim OY, Dinh NTH, Park HT, Choi SJ, Hong K, Gho YS. Bacterial protoplast-derived nanovesicles for tumor-targeted delivery of chemotherapeutics. *Biomaterials* 2017;**113**:68−79.
33. Agarwal PK, de Oliveira LC, da Silva VM, Colussi F, Cabral AD, de Oliveira Neto M, et al. Conformational changes in a hyperthermostable glycoside hydrolase: enzymatic activity is a consequence of the loop dynamics and protonation balance. *PLoS One* 2015;**10**:e0118225.
34. Zhao Z, Ma ZX, Wang B, Guan YK, Su X-D, Jiang ZF. Mn^{2+} directly activates cGAS and structural analysis suggests Mn^{2+} induces a noncanonical catalytic synthesis of 2′3′-cGAMP. *Cell Rep* 2020;**32**:108053.
35. Lim TS, Goh JKH, Mortellaro A, Lim CT, Hämmerling GJ, Ricciardi-Castagnoli P. CD80 and CD86 differentially regulate mechanical interactions of T-cells with antigen-presenting dendritic cells and B-cells. *PLoS One* 2012;**7**:e45185.
36. Trzupek D, Dunstan M, Cutler AJ, Lee M, Godfrey L, Jarvis L, et al. Discovery of CD80 and CD86 as recent activation markers on regulatory T cells by protein-RNA single-cell analysis. *Genome Med* 2020;**12**:55.
37. Gilmour BC, Corthay A, Øynebråten I. High production of IL-12 by human dendritic cells stimulated with combinations of pattern-recognition receptor agonists. *npj Vaccines* 2024;**9**:83.
38. Raskov H, Orhan A, Christensen JP, Gögenur I. Cytotoxic $CD8^+$ T cells in cancer and cancer immunotherapy. *Br J Cancer* 2020;**124**:359−67.
39. Shi YH, Hao DL, Qian H, Tao ZM. Natural killer cell-based cancer immunotherapy: from basics to clinical trials. *Exp Hematol Oncol* 2024;**13**:101.
40. Tang ZM, Liu YY, He MY, Bu WB. Chemodynamic therapy: tumour microenvironment-mediated fenton and fenton-like reactions. *Angew Chem Int Ed Engl* 2018;**58**:946−56.
41. Hu MY, Deng FY, Song XL, Zhao HK, Yan F. The crosstalk between immune cells and tumor pyroptosis: advancing cancer immunotherapy strategies. *J Exp Clin Cancer Res* 2024;**43**:190.
42. Hu JJ, Liu X, Xia SY, Zhang ZB, Zhang Y, Zhao JX, et al. FDA-approved disulfiram inhibits pyroptosis by blocking gasdermin D pore formation. *Nat Immunol* 2020;**21**:736−45.
43. Voskoboinik I, Whisstock JC, Trapani JA. Perforin and granzymes: function, dysfunction and human pathology. *Nat Rev Immunol* 2015;**15**:388−400.
44. Boutilier AJ, Elsawa SF. Macrophage polarization states in the tumor microenvironment. *Int J Mol Sci* 2021;**22**:6995.
45. Ao F, Li X, Tan Y, Jiang ZB, Yang F, Guo JP, et al. STING agonist-based hydrogel enhances immune activation in synergy with radiofrequency ablation for hepatocellular carcinoma treatment. *J Control Release* 2024;**369**:296−308.

46. Zhu XQ, Li TH, Wang Q, Yan KN, Ma SS, Lin Y, et al. Dual-synergistic nanomodulator alleviates exosomal PD-L1 expression enabling exhausted cytotoxic T lymphocytes rejuvenation for potentiated iRFA-treated hepatocellular carcinoma immunotherapy. *ACS Nano* 2024;**18**:32818−33.
47. Zeng GC, Liang XY, Ling Y, Zhu XQ, Wang Q, Li ZL, et al. Tumor vascular occlusion by calcium-based thermosensitizer provokes continuous cavitation effect and thermal energy transition efficiency of radiofrequency ablation therapy. *Biomaterials* 2025;**315**:122944.
48. Garris CS, Luke JJ. Dendritic cells, the T-cell-inflamed tumor microenvironment, and immunotherapy treatment response. *Clin Cancer Res* 2020;**26**:3901−7.
49. Xia JY, Wang LY, Shen TL, Li P, Zhu PY, Xie SN, et al. Integrated manganese (III)-doped nanosystem for optimizing photothermal ablation: amplifying hyperthermia-induced STING pathway and enhancing antitumor immunity. *Acta Biomater* 2023;**155**:601−17.
50. Li WW, Lu L, Lu JJ, Wang XR, Yang C, Jin JS, et al. cGAS−STING-mediated DNA sensing maintains $CD8^+$ T cell stemness and promotes antitumor T cell therapy. *Sci Transl Med* 2020;**12**:eaay9013.
51. Marcus A, Mao AJ, Lensink-Vasan M, Wang L, Vance RE, Raulet DH. Tumor-derived cGAMP triggers a STING-mediated interferon response in non-tumor cells to activate the NK cell response. *Immunity* 2018;**49**:754−63.e4.
52. Wang CG, Guan YK, Lv MZ, Zhang R, Guo ZY, Wei XM, et al. Manganese increases the sensitivity of the cGAS−STING pathway for double-stranded DNA and is required for the host defense against DNA viruses. *Immunity* 2018;**48**:675−87.e7.
53. Masoud GN, Li W. HIF-1α pathway: role, regulation and intervention for cancer therapy. *Acta Pharm Sin B* 2015;**5**:378−89.
54. Levantini E, Maroni G, Del Re M, Tenen DG. EGFR signaling pathway as therapeutic target in human cancers. *Semin Cancer Biol* 2022;**85**:253−75.
55. Geng PY, Ye F, Dou P, Hu CX, He JR, Zhao JH, et al. HIF-1α−HPRT1 axis promotes tumorigenesis and gefitinib resistance by enhancing purine metabolism in EGFR-mutant lung adenocarcinoma. *J Exp Clin Cancer Res* 2024;**43**:269.
56. Wang Q, Zhu XQ, Yin BX, Yan KN, Qiu GH, Liang XY, et al. Multi-hierarchical Fe single atom nanozymes with axially-coordinated O-Fe-N4 active centers reshape macrophage epigenetics against immunosuppression. *Adv Funct Mater* 2024;**34**:2408141.
57. Rosenberg J, Huang J. $CD8^+$ T cells and NK cells: parallel and complementary soldiers of immunotherapy. *Curr Opin Chem Eng* 2018;**19**:9−20.
58. Herault A, Mak J, de la Cruz-Chuh J, Dillon MA, Ellerman D, Go M, et al. NKG2D-bispecific enhances NK and $CD8^+$ T cell antitumor immunity. *Cancer Immunol Immunother* 2024;**73**:209.
59. Wright SS, Kumari P, Fraile-Ágreda V, Wang CL, Shivcharan S, Kappelhoff S, et al. Transplantation of gasdermin pores by extracellular vesicles propagates pyroptosis to bystander cells. *Cell* 2025;**188**:280−91.
60. Wu SP, Wang BJ, Li HZ, Wang HF, Du SL, Huang X, et al. Targeting STING elicits GSDMD-dependent pyroptosis and boosts antitumor immunity in renal cell carcinoma. *Oncogene* 2024;**43**:1534−8.
61. Wu AA, Drake V, Huang HS, Chiu S, Zheng L. Reprogramming the tumor microenvironment: tumor-induced immunosuppressive factors paralyze T cells. *OncoImmunology* 2015;**4**:e1016700.
62. Zhang ZL, Zhou H, Ouyang XH, Dong YL, Sarapultsev A, Luo SS, et al. Multifaceted functions of STING in human health and disease: from molecular mechanism to targeted strategy. *Signal Transduct Targeted Ther* 2022;**7**:394.
63. Liu ZQ, Wang D, Zhang JR, Xiang PJ, Zeng ZY, Xiong W, et al. cGAS−STING signaling in the tumor microenvironment. *Cancer Lett* 2023;**577**:216409.
64. Overacre-Delgoffe AE, Chikina M, Dadey RE, Yano H, Brunazzi EA, Shayan G, et al. Interferon-γ drives Treg fragility to promote anti-tumor immunity. *Cell* 2017;**169**:1130−41.e11.